International Journal of Heat and Mass Transfer 173 (2021) 121211

Contents lists available at ScienceDirect

International Journal of Heat and Mass Transfer

journal homepage: www.elsevier.com/locate/hmt

Numerical study of SALSCS demonstration unit in Xi 'an, China, with non-uniform solar irradiation

Ming-Hua Huang[a], Ya-Ling He[a], Zhen-Ping Feng[b], Jun-Ji Cao[c], Wen-Quan Tao[a,*]

[a] Key Laboratory of Thermo-Fluid Science and Engineering of MOE, Xi'an Jiaotong University, Xi'an 710049, China
[b] Shaanxi Engineering Laboratory of Turbomachinery and Power Equipment, Xi'an Jiaotong University, Xi'an 710049, China
[c] Key Laboratory of Aerosol, SKLLQG, Institute of Earth Environment, Chinese Academy of Sciences, Xi'an 710061, China

ARTICLE INFO

Article history:
Received 25 January 2021
Revised 7 March 2021
Accepted 9 March 2021
Available online 15 April 2021

Keywords:
Solar-assisted large-scale cleaning system
Solar chimney
PV
Non-uniform solar radiation
CFD

ABSTRACT

Solar-Assisted Large-Scale Cleaning System (SALSCS) is a new attempt to alleviate outdoor air pollution by using solar energy. A demonstration unit was built in Xi 'an, China, in 2016. Field tests and numerical simulations were carried out on the demonstration unit in January 2017. Results show that the thermal airflow rate of the south collector is well predicted, while that of the north collector is seriously overestimated, with a deviation between the simulated value and the measured value being as larger as 47.07%. In this paper, an improved numerical simulation method considering the non-uniformity of solar irradiation, the effects of weather condition and the photovoltaic panels of the collector top is presented. Simulation results show that the deviation between the simulated thermal airflow rate of the north collector and the measured value is only 2.13%. Photovoltaic panels on the collector top have a little influence on the thermal airflow rate of the collectors. If the roof of the north and south collectors is covered with all photovoltaic panels, the thermal airflow rate will be reduced only by 6.93% and 7.99%, respectively.

1. Introduction

At present, many people of the world live and work in urban areas. According to the data issued by the United Nation, in 2018 55% of the world's population lived in cities, and that proportion is expected to increase to 68% by 2050 [1]. Cities are the centers of people's economic activities, consume huge amounts of energy and release large amounts of heat, pollution gas and particulate matters. At the same time, the rapid growth of urbanization modifies the landscape of the urban areas, leading to significant changes in local and regional climate, and resulting in many urban environmental characteristics, such as urban heat island and air pollution [2]. The development of urbanization combined with climate change has brought a severe pressure to urban air pollution control. Usually, air pollution control projects are mainly based on the pollution source control technology. For example, various techniques for efficient and clean combustion, such as desulfurization, denitrification, dust removal, and catalytic purification, have been developed for coal burning, motor vehicles and biomass combustion. Fossil fuels have being used as the main source of energy, and expected to be further used for a long time. In addition, the number of motor vehicles will be continuously increased in the world. Hence, it is difficult to completely eliminate the emission of pollutants. Therefore, we need to actively seek supplementary measures apart from the pollution source control technology. In 2015, Cao and his coworkers [3] proposed a Solar-Assisted Large-Scale Cleaning System (SALSCS), which covers an area of 19.63 km^2 and has a chimney 500 meters high. The idea of SALSCS is inspired by the Solar Chimney Power Plant (SCPP) first built in 1981 in Spain [4], with an important improvement of installing filters before air goes into the chimney. In the SALSCS the solar energy is used to generate thermal updraft air to attract the polluted air from the environment, polluted air is purified by the filters, and then purified air is vented to the environment through the chimney. One and half year later, a demonstration unit of the SALSCS was built in the city of Xi'an, China, which covers an area of 2580 m^2 and has a chimney 60 m high, being the world's first building structure to use solar energy and advanced filtration technology for outdoor air purification [5]. The differences between this demonstration unit and the SALSCS proposed by Cao et al. [3] are not only just in size, but also in technologies. The team of IEECAS (Institute of Earth Environment, Chinese Academy of Sciences) proposed that solar photocatalytic materials are covered on the glass of the collector to decompose NO_x, NH_3 and SO_2, which are the most important gaseous precursors of haze formation in the air. The team of Xi 'an Jiaotong University proposed to set solar photovoltaic (PV) panels on the top of the collector to generate thermal updraft airflow through the

* Corresponding author.
E-mail address: wqtao@mail.xjtu.edu.cn (W.-Q. Tao).

https://doi.org/10.1016/j.ijheatmasstransfer.2021.121211
0017-9310/

heat dissipation of photovoltaic panels and increase the system's power generation [6]. After the completion of the Xi'an demonstration unit, the system flow rate and the performance of various filter devices were tested for three days in January 2017.

Since SALSCS is inspired by SCPP, this paper firstly reviews the research on SCPP. Many experimental SCPP setups have been established and tested to verify the feasibility of SCPP as summarized in review literatures [7–10]. But the sizes of the chimneys of the most test set-ups are no more than 10-meter high. The first SCPP built in 1981 in Spain has been so far the largest, with a chimney height of 60 m and a solar collector radius of 122 m [4]. In order to study the influence of various environmental conditions and geometric parameters on the performance of solar chimneys, a variety of mathematical models have been established. Pasumarthi and Sherif [11] presented an approximate theoretical analysis. Padki and Sherif [12] developed a simple mathematical model to predict the performance of solar chimney system. Gannon and von Backstrom [13] used a simple model to analyze losses of the solar chimney system, including the friction loss of the chimney, wind turbine loss and the kinetic energy loss at the chimney outlet. Bernardes [14] proposed a simple model to estimate the output power of solar chimney system, and analyzed various environmental conditions and structure size effect on the output power. Pretorius and Kroger [15] added the newly developed convective heat transfer correlation and the momentum equation to their mathematical model to evaluate the performance of a large solar chimney plant. Then Bernardes et al. [16] compared and evaluated Bernardes's model [14] and Pretorius's model [15], and pointed out that it is the difference of heat transfer coefficients that leads to the discrepancies between the predictions of the two models. Zhou et al. [17] and Li et al. [18] also proposed their own theoretical model to predict the output power of the solar chimney system. This kind of theoretical model can quickly predict the output power of SCPP but cannot reflect the distribution of physical field.

In recent decades, many researches have used computational fluid dynamics (CFD) technique to simulate the flow and heat transfer inside solar chimney system and predict their output power based on solving the coupled equations of mass, momentum and energy. Due to the symmetry of solar chimneys and assuming uniform solar irradiation, many researches are based on two-dimensional CFD models. Pastohr et al. [19] used commercial software FLUENT to carry out a two-dimensional steady numerical simulation for the Manzanares pilot power plant in Spain, and compared the simulated results with a simple mathematical model. The Pastohr's model assumes that in the collector the energy fluxes from the radiation heat transfer are smaller than those from convection and heat conduction, so the radiation heat transfer is ignored in simulations. And the model deals with the incident solar radiation as the heat source on the surface of the soil layer. However, the model leads to an excessive ground surface temperature prediction, even though this model was adopted by several successive researchers [20–24]. In fact, the radiation effect should be taken into account. This is because the roof glass of the solar collector is selectively permeable to light. A piece of clear glass has a transmittance of about 90% for wavelengths less than 3 μm, and is almost opaque for those greater than 3 μm. The wavelength of solar radiation is in the range of 0.19-2.5 μm, while the wavelength of long-wave thermal radiation of the ground is in the range of 3-120 μm [25]. Therefore, the solar collector receives most of the solar radiation while intercepts the long-wave radiation of the ground, which is the greenhouse effect. The greenhouse effect caused by the radiation heat transfer in solar collector is the important reason for the upward buoyancy. Huang et al. [26] compared different two-dimensional solar load model and pointed that the practice of directly put the total solar radiation as the heat source on the surface of the soil layer will overestimate the ground surface temperature of the solar collector. In order to determine the influence of radiation heat transfer on the surface temperature field of the solar collector, Guo et al. [27,28] simulated the solar chimney system using a three-dimensional discrete ordinates (DO) radiation model and compared the results with those without radiation model. Their results showed that the ground surface temperature was too high in the absence of radiation model. Therefore, the simple solar loading model and ignoring radiation heat transfer in the solar collector are the causes of the excessive ground surface temperature for Pastohr's model. After Guo et al. 's work, some researchers [29–33] have also adopted a three-dimensional CFD model with DO radiation model in their numerical studies of solar chimneys. These numerical studies have shown that considering radiation heat transfer to simulate the greenhouse effect has an important role in accurately predicting the flow and heat transfer characteristics of the solar chimney system.

Although a large number of numerical simulation studies have been carried out on solar chimney systems and the numerical models have been improved from one-dimension to two-dimension and then to three-dimension, it should be pointed out that the current numerical models have two important deficiencies: one is that all models are based on the assumption of uniform incident solar radiation. And the other is that the existing numerical simulation studies are lack of experimental verification of large-scale models [34]. Most of the numerical models were only verified according to the experimental data in 1982 provided by the experiments of the first SCPP in Spain [35].

In this paper, a numerical simulation study is carried out on SALSCS demonstration unit in Xi 'an, China. The geometric struc-

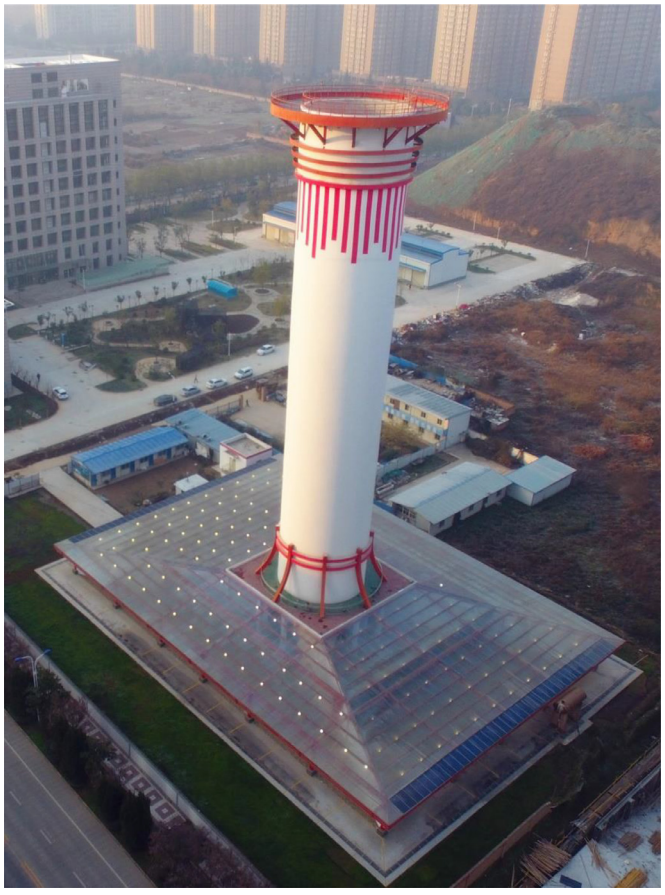

Fig. 1. Xi'an demonstration unit.

ture of the Xi'an demonstration unit is much larger than that of most SCPP setups reported in literatures, so its test data can be used to verify numerical results at a larger scale model. Cao et al. [36] built a three-dimensional steady numerical model and validated the numerical model by experimental measurement data of the demonstration unit in Xi 'an. But in their numerical model the uniform solar radiation is still assumed, and the influence of the photovoltaic panels laid on the Xi'an demonstration unit is not considered. The numerical simulation results from their model on the south side of the Xi'an demonstration unit are in good agreement with the experimental results, but the numerical simulation results on the north side have larger discrepancies with the experimental results. Cao et al. [36] also pointed out that the reason for the large deviation between the simulated results and the measured data on the north side is that the actual solar radiation received on the north side is much smaller than the adopted loading in the simulations. In this paper, an improved numerical simulation method is proposed.

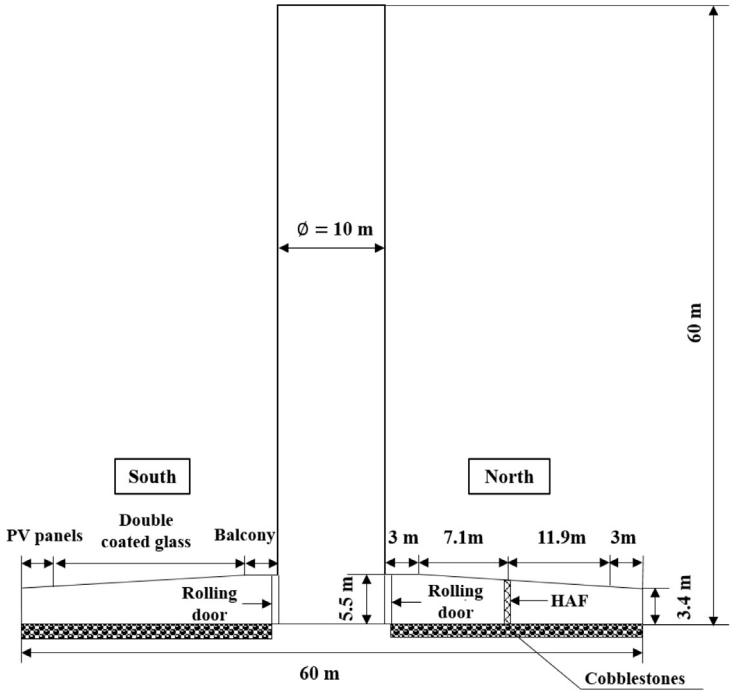

(a) South-north vertical section

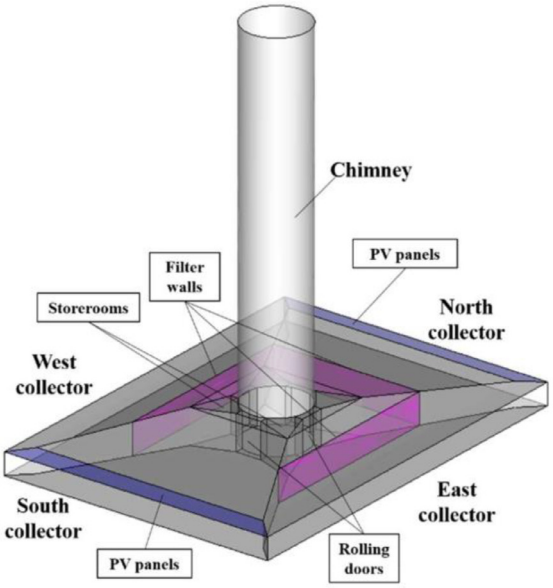

(b) Internal structure image

(c) HAF filters on the north collector

Fig. 2. Some details of Xi'an demonstration unit.

The main novelties of this paper include two aspects: the assumption of uniform incident solar radiation is abandoned and non-uniform solar irradiation is considered; the effects of weather condition and the photovoltaic panels of the collector top are taken into account.

The rest of this paper is arranged as follows. Section 2 introduces Xi'an demonstration unit and the field measurements. The numerical method is presented in Sections 3. Section 4 shows some results. Section 5 presents summary and conclusions.

2. Xi'an demonstration unit of SASLCS and field measurements

Fig. 1 shows a photo of the Xi'an demonstration unit. The south-north section size diagram, internal structure diagram and High Air Flow (HAF) filters manufactured by the 3M company on the north collector are presented in Figs. 2(a), (b) and (c), respectively. The Xi'an demonstration unit consists of a chimney with 60 meters height and a rectangle solar collector. The inner diameter of the chimney is 10 m, and the solar collector is 60 meters long from south to north and 43 meters wide from east to west. The bottom of the solar collector is covered with cobblestones to store heat during the day and release heat at night. The rectangle solar collector is divided into four parts: east, south, west and north, as shown in Fig. 2(b). Each part is connected to the chimney with a rolling door, and can be operated flexibly by controlling the opening degree of the rolling door, from fully opened to fully closed. Each part of the collector is covered by double coated tempered glass, and the upper and lower surfaces of tempered glass are coated with a thin photocatalytic film, which can remove NO_x, NH_3 and SO_2. The tempered glass is laid at an inclined angle so that the height of the collector inlet is 3.4 m and the height outlet is 5.5 m. Moreover, Photovoltaic panels with a width of 3 meters are installed at the edges of the south and north collectors, and 37 pieces of 320 W crystal silicon photovoltaic modules are equipped for each collector part. The maximum total capacity of the photovoltaic system reaches 23.7 kW. Electricity from the photovoltaic panels is first integrated into the Xi'an demonstration unit electricity system with low voltage 380 V, and the remaining electricity of the photovoltaic panels is connected to the power grid. The tempered glass is connected to the chimney by a concrete balcony with a horizontal size of 16 m $\times$ 16 m. Four enclosed triangular storerooms are located below the four corners of the concrete balcony for the storage of experimental equipment. Three different filter walls are installed at the mid-way section of the east, west and north collectors, while the south collector is set as the control group without the filter wall. The filter walls installed in the east and west collectors are characterized by high pressure drop, so each part is installed a fan to assist the system air intake. The HAF filters manufactured by the 3M company are installed in the north collector, as shown in Fig. 2(c), which has a lower pressure drop than normal filters, and the thermal airflow generated by the solar energy can pass through the HAF filters without a fan.

Measurement experiments were carried out on the Xi'an demonstration unit from 11 January to 13 January 2017, with the main purpose of assessing the capacity of the thermal updraft generation, verifying the numerical model and testing filter systems. So, the air flow rate of the south and north collectors without fans were measured. The velocity distributions in the vertical cross section between the solar collector inlet and the chimney center, and in the vertical plane of the rolling gate are measured. During the measurement, the two measuring surfaces are divided into 48 and 20 measuring points, respectively. A Gill WindSonic portable wind sensor was used to measure the wind speed normal the cross section at each measuring point. The average of the two sections flow rate was taken as the thermal flow rate of the measured collector. Kestrel 4000 portable weather instrument was used to measure the air flow temperature, and temperatures of 20 measuring points in the vertical plane of the rolling gate were measured. A MAWS201 automatic weather station was installed on the roof of a three-meter-high building next to the Xi'an demonstration unit to monitor net solar radiation and ambient temperature. The total flow rate of a measured section is determined by

$$Q = \sum_i u_i A_i \tag{1}$$

where, Q is the total volume flow rate of the measured section; u_i is the wind speed at the i^{th} measurement point perpendicular to the measured surface; A_i is the area where the i^{th} measurement point is located. The volume flow rate is the major parameter for the evaluation of the SALSCS performance.

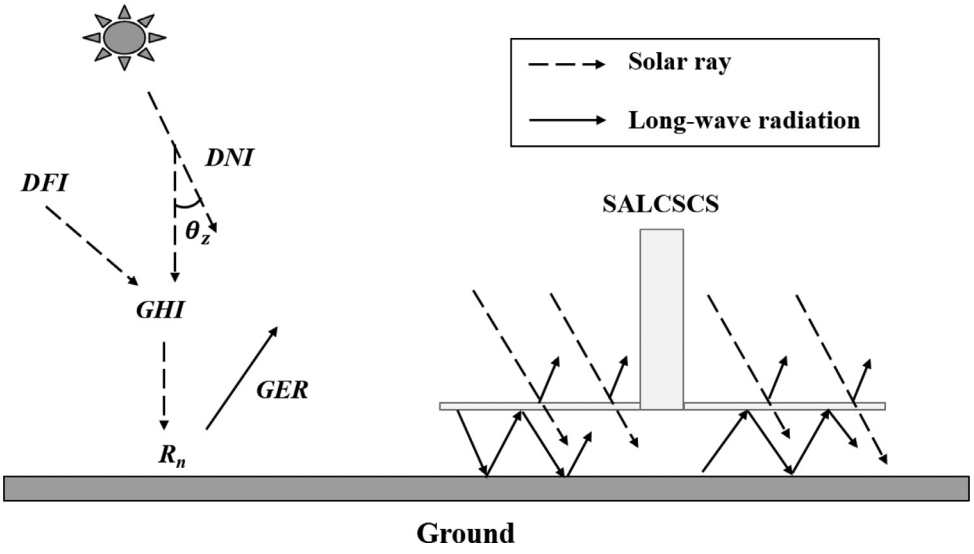

Fig. 3. Schematic diagram of solar radiation and thermal radiation in the collector.

3. Numerical method

3.1. Mathematical formulation

The airflow in the SCPP is considered as an incompressible and buoyancy driven flow. The flow strength can be measured by the Rayleigh number defined below:

$$Ra = \frac{g\beta \Delta T L^3}{\nu a} \tag{2}$$

here, ΔT is the maximum temperature difference of the system; L is the characteristic length equal to the mean height of the collector; β is the air thermal expansion coefficient, taking the inverse of the ambient temperature in K; ν is the air viscosity;α is the air thermal diffusion coefficient. The value of Rayleigh number less than 10^8 means laminar flow, and greater than 10^{10} means turbulent flow [25,36]. For the scale of the Xi'an demonstration unit, the *Ra* number based on the average collector height of all simulation cases is larger than 10^{10}, indicating that the flow field is turbulent. The Reynolds-averaged Navier-Stokes equations are employed to simulate the airflow in the Xi'an demonstration unit.

It is assumed that during the simulation period, the solar chimney system is in steady state, the fluid flow is incompressible and the Boussinesq assumption [37] is adopted to deal with the buoyancy effect. Then the governing equations for the conservation of mass, momentum and energy are as follows:

$$\frac{\partial U_i}{\partial x_i} = 0 \tag{3}$$

$$U_j \frac{\partial U_i}{\partial x_j} = -\frac{1}{\rho}\frac{\partial P}{\partial x_i} + \nu \frac{\partial^2 U_i}{\partial x_j \partial x_j} - \frac{\partial}{\partial x_j}\left(\overline{u'_i u'_j}\right) - g_i \beta (T - T_0) \tag{4}$$

$$U_j \frac{\partial T}{\partial x_j} = a \frac{\partial^2 T}{\partial x_j \partial x_j} - \frac{\partial}{\partial x_j}\left(\overline{u'_j T'}\right) + S_h \tag{5}$$

here, x_i indicates the i^{th} Cartesian coordinate (i = 1,2,3), U_i indicates the time-averaged velocity component, u'_i is the fluctuation from the i^{th} mean velocity component, $\overline{u'_i u'_j}$ denotes the Reynolds stresses and $\overline{u'_j T'}$ is the turbulent heat flux, and S_h denotes the source terms of the energy equation, which will be used to consider the energy loss caused by photovoltaic panel power generation in this paper.

In this paper the standard k-ε model is adopted. Transport equations for the turbulent kinetic energy k and turbulent kinetic energy dissipation rate ε can be described as

$$U_j \frac{\partial k}{\partial x_j} = \frac{\partial}{\partial x_j}\left[\left(\nu + \frac{\nu_t}{\sigma_k}\right)\frac{\partial k}{\partial x_j}\right] - \overline{u'_i u'_j}\frac{\partial u_i}{\partial x_j} + G_b - \varepsilon \tag{6}$$

$$U_j \frac{\partial \varepsilon}{\partial x_j} = \frac{\partial}{\partial x_j}\left[\left(\nu + \frac{\nu_t}{\sigma_\varepsilon}\right)\frac{\partial \varepsilon}{\partial x_j}\right] - C_{\varepsilon 1}\frac{\varepsilon}{k}\left(\overline{u'_i u'_j}\frac{\partial u_i}{\partial x_j} + C_{\varepsilon 3} G_b\right) - C_{\varepsilon 2}\frac{\varepsilon^2}{k} \tag{7}$$

where,

$$G_b = \beta g_i \frac{\nu_t}{\sigma_t}\frac{\partial T}{\partial x_i} \tag{8}$$

$$C_{\varepsilon 3} = \tanh\left|\frac{v}{u}\right| \tag{9}$$

The turbulent stress and heat flux can be expressed by

$$\overline{u_i' u_j'} = \frac{2}{3}k\delta_{ij} - \nu_t\left(\frac{\partial u_i}{\partial x_j} + \frac{\partial u_j}{\partial x_i}\right) \tag{10}$$

$$\overline{u_j' T'} = \frac{\nu_t}{\sigma_t}\frac{\partial T}{\partial x_j} \tag{11}$$

where,δ_{ij}represents the Kronecker delta, and$\nu_t$is the turbulent viscosity that can be determined by:

$$\nu_t = C_\mu \frac{k^2}{\varepsilon} \tag{12}$$

In the above equations, constants C_μ, $C_{\varepsilon 1}$, $C_{\varepsilon 2}$, σ_k andσ_ε are specified as 0.09, 1.44, 1.92, 1.0 and 1.3, respectively [38,39].

Come here to discuss thermal radiative heat transfer in the collector. A schematic diagram of the solar radiation and thermal radiation in the collector is shown in Fig. 3. The net solar radiation

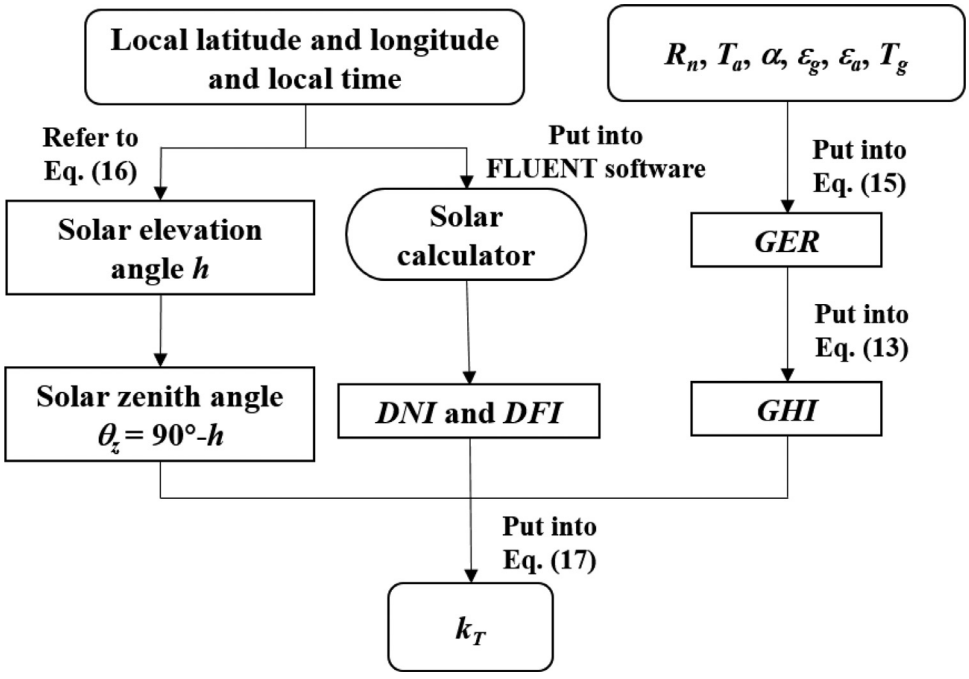

Fig. 4. Flow chart of solving sunshine fraction k_T.

received by the open ground denoted by R_n is the difference between the total solar radiation absorbed by the ground surface and the ground effective radiation, as shown below:

$$R_n = (1-\alpha)GHI - GER \tag{13}$$

$$GHI = DNI \cdot \cos(\theta_z) + DFI \tag{14}$$

$$GER = \varepsilon_g \sigma T_g^4 - \varepsilon_a \sigma T_a^4 \tag{15}$$

where, α is surface albedo (reflectance); *GHI* is the global horizontal solar irradiation; *GER* is the ground effective radiation; *DNI* is the direct normal solar irradiation; *DFI* is the diffuse horizontal solar irradiation; ε_g is the ground emissivity; T_g is the ground temperature; ε_a is the atmospheric emissivity; T_a is the atmospheric temperature; σ is the Stefan-Boltzmann constant, 5.67×10^{-8} $W \bullet m^{-2} \bullet K^{-4}$; θ_z is the solar zenith angle that is the angle between the zenith line (pointing straight up) and the direction to the sun and is the complementary angle to the solar elevation angle. The solar elevation angle, denoted by h, can be expressed by the following formula:

$$\sin h = \sin\delta \sin\varphi + \cos\delta \cos\varphi \cos t \tag{16}$$

here, t is the solar hour angle; δ is the solar declination; φ is the local latitude. t and δ are related to the local latitude and longitude, and the local time. The details of the calculation of t and δ can be found in [40].

Many studies take the full solar irradiation as the radiation received by the ground surface of the collector [19–24]. Cao et al. [36] use the measured net solar radiation as the radiation received by the ground surface of the collector when simulating the Xi'an demonstration unit. However, as shown in Fig. 3 the radiation received by the ground of the collector is the solar radiation passed through the glass, and part of the long-wave radiation was intercepted by the glass. It is obvious that the radiation received by the ground surface of the collector is not the full solar irradiation or the net solar radiation. In addition, the received solar radiation is not evenly distributed due to the angle of the sun and shadows of buildings. How to determine the amount of solar radiation received by a solar chimney system is a prerequisite for accurate simulation of system performance. In this paper, the solar ray tracing approach in ANSYS FLUENT is used to predict the irradiation of sunlight, and S2S (Surface-to-Surface) radiation model is used to simulate the thermal radiation heat transfer in the collector. A solar calculator provided by ANSYS FLUENT is used to compute the *DNI* and *DFI* according to the longitude and latitude of Xi'an demonstration unit (108.89°E, 34.16°N), the time zone (GMT+8), and the specific time of the experiments (From January 11, 2017 to January 13, 2017). And the default solar irradiation method (Fair Weather Conditions) is employed with some correction of weather condition developed by the present authors. The correction of weather condition considers the difference of the specific weather condition of the test day from the Fair Weather Conditions. In fact, during the period of the system measurement, Ref. [36] pointed out that the weather was cloudy on January 11 and sunny next two days. In this paper, the weather condition is taken into account and the parameter k_T of ANSYS FLUENT is used to modify the "Fair Weather Conditions". The global horizontal solar irradiation *GHI* is modified as shown below:

$$GHI = k_T \cdot DNI \cdot \cos(\theta_z) + DFI \tag{17}$$

The way for determining the sunshine fraction k_T is presented in Fig. 4. The solar zenith angle θ_z is derived from the solar elevation angle *h*. *DNI* and *DFI* are computed by the solar calculator of ANSYS FLUENT under "Fair Weather Conditions". *GHI* can be estimated according to the Eq. (13), where the net solar radiation R_n is the measured value from the MAWS201 automatic weather station next to the Xi'an demonstration unit and the ground effective radiation *GER* can be derived by Eq. (15). The atmospheric temperature T_a is the measured value too. The surface albedo α and the ground emissivity are set to 0.8, the atmospheric emissivity ε_a is set to 0.35 and the ground temperature outside the collector T_g refers to the simulated ground surface temperature. Then k_T can be obtained by putting θ_z, *DNI*, *DFI* and *GHI* into Eq. (17).

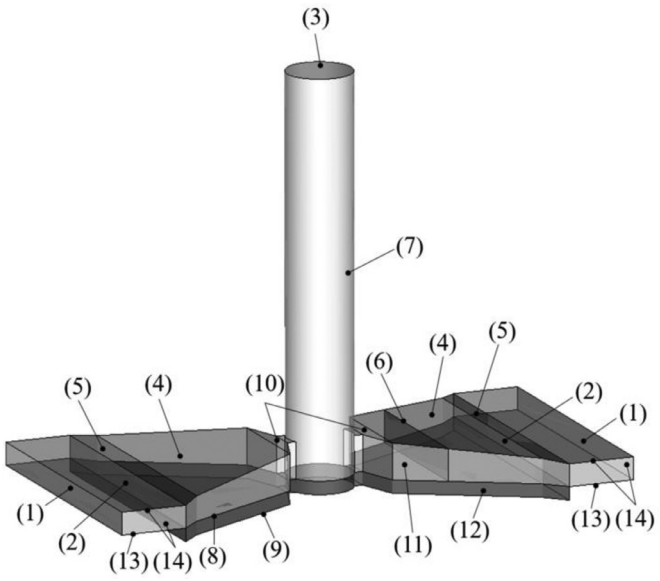

Fig. 5. Computational domain for Xi'an demonstration unit: (1) Inlet of the computational domain; (2) Actual inlet of the collectors; (3) Chimney outlet; (4) Glass; (5) PV panels; (6) HAF filters; (7) Chimney; (8) Ground surface; (9) Bottom surface of the soil layer; (10) Balcony; (11) Partition wall; (12) Side surface of the soil layer; (13) The bottom of extended region; (14) Other surfaces of extended region. The corresponding boundary conditions are illustrated in Table 1.

3.2. Computational domain and boundary conditions

The experimental measurements were only conducted for the north and south collectors, hence, the same regions are taken as the computational domain (see Fig. 5). When the south collector is running alone, the rolling door at the north side is closed and it is simulated by the wall boundary. The computational domain is divided into fluid domain and solid domain. The solid domain is used to simulate the soil layer with a thickness of 2 meters where only heat conduction plays a role. Our preliminary studies show that two meters are thick enough for heat conduction simulation within the ground soil. The fluid domain includes south collector, north collector and the chimney, where the air flows under the influence of buoyancy force. In order to adopt uniform inlet air flow condition, the fluid computational domain is extended outward 10 meters from the actual collector inlet, as shown by number 13 and 14 in Fig. 5. It is to be noted that the flow boundary conditions of the extended region are set as follows: the bottom is set as wall boundary, and the other three walls are taken as symmetry boundary. The boundary conditions for different components of the demonstration unit shown in Fig. 5 are listed in Table 1. For the PV panels, negative sources $Q_{pv,elec}$ are added to consider the energy loss caused by the PV power generation [6]. This negative source term can be determined according to following consideration. The actual power output of PV panels is related to solar irradiation and PV panel temperature. Since the experiment was carried out in winter and the cooling environment for the PV panels was good, the influence of the PV panel temperature on the power output in this calculation is ignored. Therefore, the power output

Table 1
Boundary conditions for the numerical model of the Xi'an demonstration unit.

No.	Location	Boundary condition	Value
(1)	Inlet of the computational domain	Pressure inlet	Ambient pressure and temperature
(2)	Actual inlet of the collectors	Interior	-
(3)	Chimney outlet	Pressure outlet	$P_{gage} = 0$ Pa
(4)	Glass	No-slip boundary Mixed wall	$h = 8$ W•m^{-2}•K^{-1}; Ambient pressure
(5)	PV panels	No-slip boundary Mixed wall	$h = 8$ W•m^{-2}•K^{-1}; Ambient pressure $Q_{pv,elec}$ calculated by Eq. (19)
(6)	HAF filters	Pressure drop	ΔP calculated by Eq. (20)
(7)	Chimney	No-slip boundary Adiabatic	$q = 0$ W•m^{-2}
(8)	Ground surface	No-slip boundary Coupled wall	-
(9)	Bottom surface of the soil layer	Constant temperature	4 °C higher than the ambient temperature
(10)	Balcony	No-slip boundary Adiabatic	$q = 0$ W•m^{-2}
(11)	Partition wall	No-slip boundary Adiabatic	$q = 0$ W•m^{-2}
(12)	Side surface of the soil layer	Adiabatic	$q = 0$ W•m^{-2}
(13)	The bottom of extended region	No-slip boundary Constant temperature	Ambient temperature
(14)	Other surfaces of extended region	Symmetry	-

of the PV panels can be regarded as a linear correlation with the received solar radiation. The designed peak output power of each PV panel is 320 W, so the actual power output of each PV panel and the related source term can be calculated by Eqs. (18) and (19), respectively.

$$P_{PV} = \frac{G_{PV}}{1000} \cdot 320, \tag{18}$$

$$Q_{pv,elec} = -\frac{P_{PV}}{A_{PV}\delta_{PV}}, \tag{19}$$

where, G_{pv} is the actual solar radiation received by each PV panel, in W•m^{-2}; A_{PV} is the area of the PV panel, in m^2; δ_{PV} is the thickness of the PV panel, in m. Since the solar radiation received by each PV panel is not uniform and the power generation of different PV panel is uneven, so the negative sources are also non-uniform.

A pressure resistance is employed to simulate the HAF filters. According to the experimental data on the installed HAF filter media of the Xi'an demonstration unit, the pressure drop of the HAF filters is fitted as a function of the face velocity [36], as shown below:

$$\Delta P = 4.39v^2 + 5.20v \tag{20}$$

where, v is the face velocity.

3.3. Solver settings

The 3D steady RANS equations with standard k-ε turbulence closure are solved by ANSYS FLUENT 14.0. The solar ray tracing model is adopted to predict the incident solar energy from the sun, and the parameter k_T of ANSYS FLUENT is defined to consider the influence of the weather situation. As indicated above, a program for calculating k_T is developed based on the Python language according to Fig. 4. The sunlight transmissivity of glass and PV panels is set at 0.8 and 0 respectively and the absorptivity of glass and PV panels is set at 0.04 and 0.855 respectively. The S2S radiation model is used to simulate the thermal radiation in the collector. Boussinesq approximation is applied to reflect the buoyancy effect. The pressure-velocity coupling is dealt with by the SIMPLE algorithm. The second-order upwind discretization scheme is selected for the convection terms and central difference for the diffusion terms. Full-hexahedral grids are generated for the simulations, which can well adapt the geometry of the simulated system. By monitoring the system volume flow rate, three sets of mesh have been examined for a mesh independence of numerical solutions, which have the total cell number of 659416, 1582612 and 5825034, respectively. The numerical deviation between the second set and the finest mesh is less than 2% of the total volume flow rate. So, the mesh with the total cell number of 1582612 is selected. And the distance from the first layer grids to the wall is sufficiently small to guarantee that the Y^+ is in the range of 30 to 300. The local grid distributions near the collector outlet and around the connection part of collector and chimney are shown in Fig. 6. All simulations are performed on Inspur high performance computing cluster of authors' research group with 32 cores. Every simulation lasts for about 10 hours.

4. Results and discussion

In this section, the numerical results are first compared with the test results and the numerical results reported in Ref. [36]. Then the predicted power outputs from the PV panels of the south and north collectors are presented. Finally, the effect of covering PV panel on the thermal air flow rate of the system is discussed.

4.1. Comparisons analysis of uniformity of absorbed solar radiation

The measurement conditions are listed in Table 2. All cases are at midday, when the air flow can be approximately regarded as steady. CASE 2 and CASE 3 are at the same experimental period. CASE 2 presents the results of the south collector, while CASE 3 the north collector. As mentioned earlier, it is assumed that the solar chimney system is stable during the simulation period. So in simulations the middle times of the experimental periods is used to compute the solar load, which are 11:45 a.m. of January 11, 11:35 a.m. of January 12 and 10:35 a.m. of January 13.

Fig. 7 shows the measured data and numerical results of the thermal airflow rate and the temperature at the rolling door from the present simulation and from Ref. [36]. The deviations between the measured data and numerical results are evaluated by RMSE, as shown in Eq. (21).

$$\mathrm{RMSE} = \sqrt{\frac{1}{n}\sum_1^n (C_o - C_p)^2} \tag{21}$$

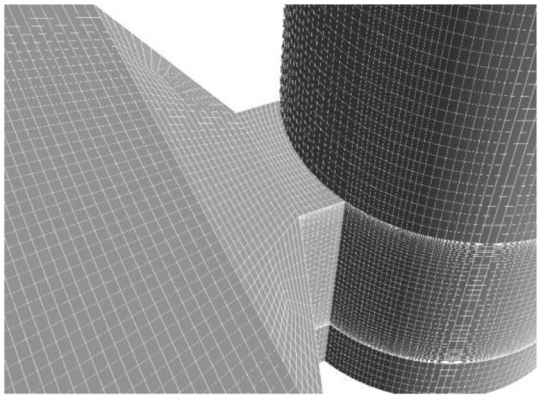

(a) Grid distibution near the collector outlet

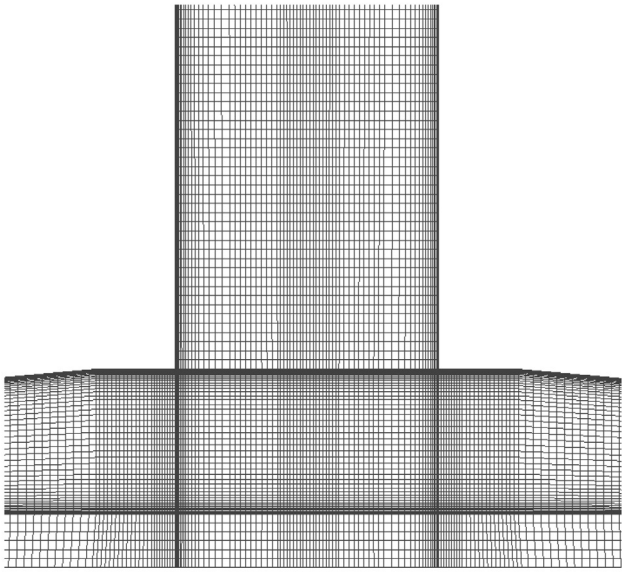

(b) Grid distibution at the vertical section around the connection part of collector and chimney

Fig. 6. Local grid distributions of the numerical model for Xi'an Demonstration Unit.

Table 2
Experimental conditions and environmental parameters.

CASE	Experimental period (Local Beijing time)	Operation conditions	Measured collector	Rn $W \bullet m^{-2}$	T_a ^oC
CASE 1	January 11 11:17 a.m. – 12:10 noon	Both north and south collectors operated	South	108.68	4.59
CASE 2	January 12 10:48 a.m. – 12:20 noon	Both north and south collectors operated	South	262.68	6.77
CASE 3	January 12 10:48 a.m. – 12:20 noon	Both north and south collectors operated	North	262.68	6.77
CASE 4	January 13 10:10 a.m. – 11:00 a.m.	Only south collector operated	South	166.23	3.88

here C_o refers to the observed value, C_p represents the simulation value, and n is the number of the measurements.

For the numerical model of Ref. [36], RMSE values between simulated and observed values for the volumetric flow rate and temperature of the four cases are 5.32 $m^3 \bullet s^{-1}$ and 1.66 °C, respectively. And for the present numerical model, RMSE values are 2.22 $m^3 \bullet s^{-1}$ and 1.09 °C, respectively. It can be seen that the numerical model proposed in this paper is more accurate.

As can be seen from Fig. 7, simulation results of the south collector (CASES 1, 2 and 4) by numerical model of Ref. [36] and the present numerical model are both in good agreement with the experimental results. However, the predicted thermal flow rate of the north collector (CASE 3) by Ref. [36] is much higher than the measured value, with a deviation of 47.07%, while the deviation of this paper is only 2.13%. This is because the two models are different in dealing with solar load and thermal radiation in the collector. As indicated above, the model of Ref. [36] evenly loads the observations of net ground radiation at the bottom of the collector. The present model takes into account the solar incidence by using ray tracing, calculates the solar irradiation entering the collector

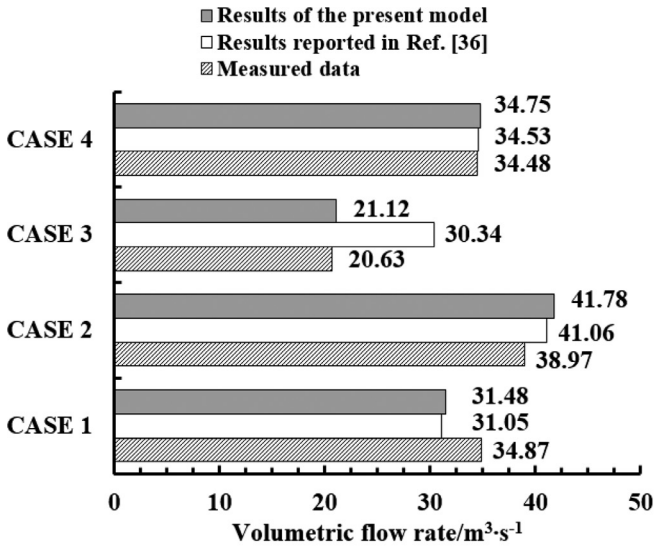

(a) Volumetric flow rate

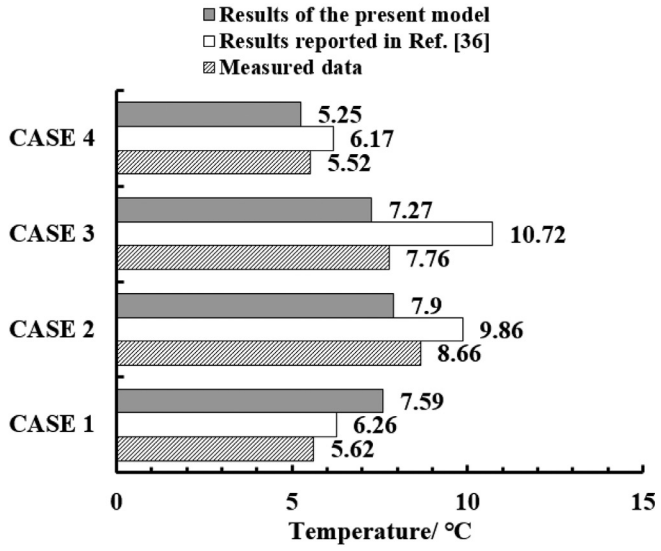

(b) Average temeperature at the rolling door

Fig. 7. Comparison of measured data and simulated results.

by setting the sunshine fraction k_T and glass transmission, and intercepts the long-wave radiation of the collector by using the S2S radiation model. Fig. 8 shows the sunshine fraction k_T and solar irradiation absorbed by the bottom and top of the collectors during the three experimental periods. It can be seen that k_T of January 11 is smaller than that of the other two days, which is caused by the weather on January 11 being less sunny than that of the next two days. Fig. 8 also presents the cloud map of the absorbed solar radiation. Take the result of January 12 shown on Fig. 8(b) for instance. From Fig. 8(b) it can be seen that the glass of the collector top penetrates most of the sunlight and the values of the top absorbed radiation is low hence the corresponding cloud map appears blue, while the PV panels of the south collector absorb much more sunlight and appear red in the cloud map. But the PV panels of the north collector appear mostly green and partly blue in the cloud map due to the angle of incidence of the sun and the shadow of the chimney. At the bottom of the collectors, except for the part shaded by the PV panels, the solar radiation on the south collector is quite uniform, while the sunshine on the north collector is very non-uniform and in many local areas the absorbed solar radiation is quite low. This is the reason why the thermal air flow rate of the north collector is seriously overestimated by loading uniform solar radiation in Ref. [36]. The practice of Ref. [36] shows that taking the net absorption of the solar radiation being the absorbed solar energy of the collector can give fairly good simulation results of the south collector while seriously overestimates the airflow rate of the north collector.

Fig. 9 shows the simulated air streamlines inside the demonstration unit for CASE 2 and CASE 3 measured on January 12. It can be found that the air inflow of the south collector is more trimly without backflow. While flow in the north collector shows more random characteristics, leading to its weak ability to produce thermal updraft.

From above discussion, it can be concluded that generally speaking in order to establish more accurate simulation model, the assumption of uniform incident solar radiation should be abandoned and the effects of weather condition and some other conditions (say shadow of the chimney) should be taken into account.

Table 3
The total power output and operating efficiency of photovoltaic panels.

Time	Installation location	Total power output kW	Operating efficiency
January 11	South collector	4.63	39.07%
	North collector	2.69	22.69%
January 12	South collector	6.23	52.60%
	North collector	3.44	29.01%
January 13	South collector	4.92	41.51%
	North collector	2.91	24.58%

4.2. Analysis of power output of PV panels

Another difference between the present study and the numerical model of Ref. [36] is that the paper takes into account the power generation of PV panels. Table 3 lists the predicted power output of PV panels under experimental conditions and the operating efficiency percentage against the designed peak power output. The predicted operating efficiency of the PV panels installed on the south collector on sunny days on January 12 and 13 is between 40% to 50%, and the operating efficiency can reach 39.07% even on cloudy days on January 11. However, the PV panels installed on the north collector have less power output. It can be found that the operating efficiency of PV panels installed on the north collector is about half as that of PV panels installed on the south collector under the same lighting conditions. The main reason is that PV panels on the north side receive less solar radiation, while the PV panels installed on the south collector receive more and uniform solar radiation, as shown in Fig. 8. The installation angle of the PV panels of the demonstration unit is about 5°, which is not the optimal installation angle provided by the manufacturer. According to the estimation of the photovoltaic manufacturer, the annual average operating efficiency of the whole photovoltaic power generation system with the installation angle of 5°, including the south and north side, is 48%. As mentioned above only steady simulations are conducted, and the midday operating efficiencies of the photovoltaic power generation system are predicted. The whole operating efficiencies of south and north side on January 11, 12 and 13 in winter are 30.88%, 40.81% and 33.05%, respectively. To some extent, the simulated results are in good agreements with the annual average estimation from the manufacturer. It should be noted that during the measurement of the demonstration unit the electricity generated by the PV panels was not special recorded, thus the predicted efficiency values can only be compared with the one provided by the manufacturer.

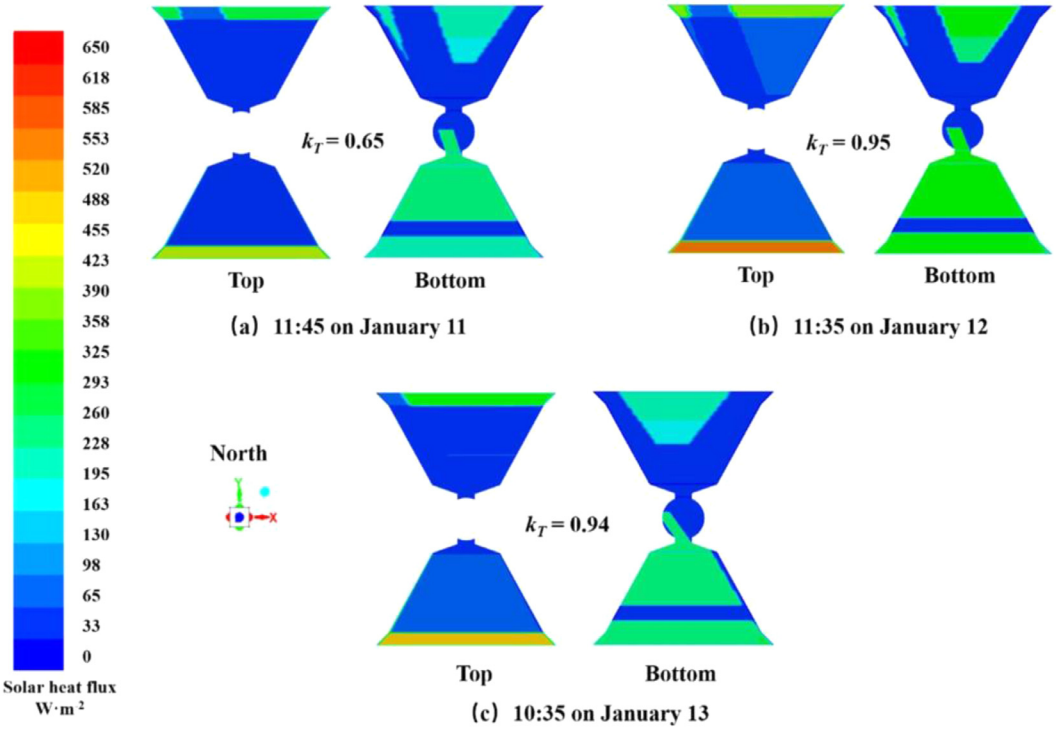

Fig. 8. Cloud map of the absorbed solar radiation of the north and south collectors and the sunshine fraction k_T.

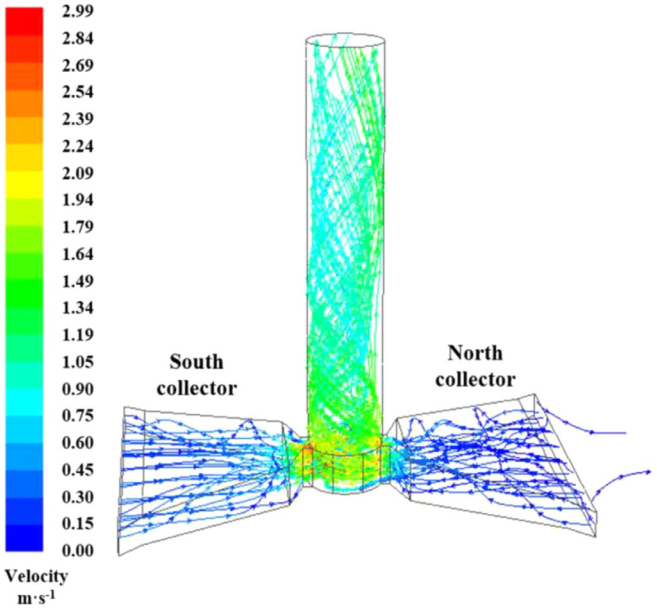

Fig. 9. The streamlines for south and north collectors of CASE 2 and CASE 3.

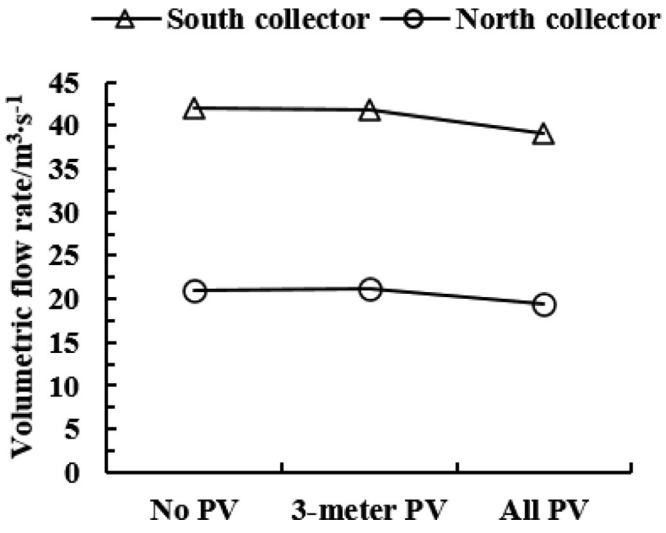

Fig. 10. The influence of photovoltaic panels on the thermal airflow rate.

4.3. Analysis of the influence of PV panels on thermal air flow rate

This paper also analyzes the influence of PV panels on the thermal airflow rate of the collectors. For the working condition on January 12, the situation without PV panels and the situation where the roof of the collector is all covered with PV panels are simulated, and the results are shown in Fig. 10. It can be found that the 3-meter-wide PV panels at the edge of the collector have a little influence on the thermal flow rate of the system. 3-meter-wide PV panels make the thermal flow rate of the south collector decrease by 0.55%, while make the thermal flow rate of the north collector increase by 0.43%. When all the collector top surface is covered by PV panels, the thermal flow rate of the south and north collectors only decreases by 6.93% and 7.99%, respectively. While the output power of PV panels on the south and north collectors reaches 30.42 kW and 15.56 kW respectively and the operating efficiency is 49.63% and 25.38% respectively. If this electricity is used to drive a fan, the generated air flow rate will much larger than the reduced value (about several $m^3 \bullet s^{-1}$ as shown in Fig. 10).

The influence of photovoltaic panels on the absorbed solar radiation of the bottom ground is presented in Fig. 11. From Fig. 11 (a) and (b), it can be seen that the shielding effect of 3-meter-wide PV panels install on the south collector affects the absorption of solar radiation on the ground surface, while 3-meter-wide PV panels in-

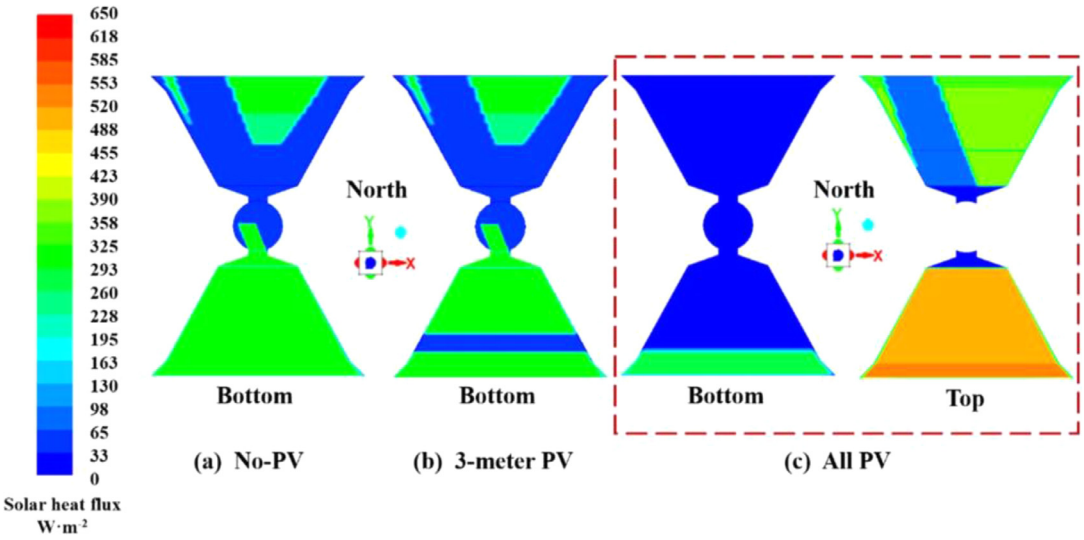

Fig. 11. The influence of photovoltaic panels on the absorbed solar radiation.

stall on the north collector do not affect the solar radiation distribution of the ground surface, but the heat dissipation of PV panels increases the thermal flow rate of the north collector. Fig. 11 (c) reflects the collector bottom and top absorbed solar irradiation when the roof of the collector is all covered with PV panels. It can be seen that except for the incoming solar radiation from the inlet of the south collector there is no solar radiation at the bottom of the collector due to the shielding of the photovoltaic panels and balcony on the top of the collector. So the collector mainly relies on the heat dissipation of PV panels to generate thermal air flow. However, the thermal flow rate of the south and north collectors decreases by less than 10 percentage, as shown above.

5. Summary and conclusions

In this paper, an improved numerical method is proposed for the simulation of SALSCS demonstration unit in Xi 'an, China, which considers the non-uniformity of solar irradiation and the effects of weather condition and the photovoltaic power generation. The main conclusions are as follows:

(1) For the SCPP numerical simulation, the assumption of uniform incident solar radiation should be abandoned and the effects of weather condition and some other conditions (say shadow of the chimney) should be taken into account. Under the assumption of uniform incident solar radiation, the simulated thermal airflow rate of the north collector of the demonstration unit in Xi 'an is seriously overestimated by 47.07%, while the deviation of the present method is only 2.13%.

(2) PV panels on the collector top have a little influence on the thermal airflow rate of the collectors. 3-meter-wide PV panels at the edge of the collectors decrease the thermal airflow rate of the south collector by 0.55%, while increase the thermal airflow rate of the north collector by 0.43%. After replacing all roof glass to PV panels, the thermal airflow rate decreases only by 6.93% and 7.99%, respectively. If the electricity by PV panels is used to drive a fan the generated air flow rate will much larger than the reduced value.

(3) The operating efficiency of PV panels on the north collector of the demonstration unit in Xi 'an is about half as that of PV panels on the south collector under the same solar radiation conditions. In January, on the sunny day the operating efficiency of PV panels on the south collector is between 40% to 50%, and even on the cloudy day the operating efficiency can reach 39.07%.

Declaration of Competing Interest

The authors declare that they have no known competing financial interests or personal relationships that could have appeared to influence the work reported in this paper.

CRediT authorship contribution statement

Ming-Hua Huang: Conceptualization, Software, Investigation, Validation, Data curation, Writing – original draft. **Ya-Ling He:** Supervision. **Zhen-Ping Feng:** Supervision. **Jun-Ji Cao:** Supervision. **Wen-Quan Tao:** Resources, Funding acquisition, Writing – review & editing.

Acknowledgments

The authors would like to acknowledge the support provided by the Foundation for Innovative Research Groups of the National Natural Science Foundation of China (No.51721004), the Key Research Program of the Chinese Academy of Sciences (Approved on 8 August, 2014) and the 111 Project (B16038).

References

[1] United Nations, World urbanization prospects: the 2018 revision, The United Nations' Department of Economic and Social Affairs-Population Division, New York, 2018.
[2] J. Song, Z.H. Wang, Interfacing the urban land–atmosphere system through coupled urban canopy and atmospheric models, Bound.-Layer Meteorol. 154 (2015) 427–448.
[3] Q. Cao, D.Y.H. Pui, W. Lipiński, A Concept of a novel solar-assisted large-scale cleaning system (SALSCS) for urban air remediation, Aerosol Air Qual. Res. 15 (1) (2015) 1–10.
[4] W. Haaf, K. Friedrich, G. Mayr, J. Schlaich, Solar chimneys - Part I: principle and construction of the pilot plant in Manzanares, Int. J. Sol. Energy 2 (1) (1983) 3–20.
[5] D. Cyranoski, China tests giant air cleaner to combat urban smog, Nature 555 (2018) 152–153.
[6] M.H. Huang, L. Chen, L. Lei, P. He, J.J. Cao, Y.L. He, Z.P. Feng, W.Q. Tao, Experimental and numerical studies for applying hybrid solar chimney and photovoltaic system to the solar-assisted air cleaning system, Appl. Energy 269 (2020) 115–150.
[7] X.P. Zhou, Y.Y. Xu, Solar updraft tower power generation, Sol Energy 128 (2016) 95–125.
[8] N. Monghasemi, A. Vadiee, A review of solar chimney integrated systems for space heating and cooling application, Renew. Sustain. Energy Rev. 81 (2) (2017) 2714–2730.

[9] A.B. Kasaeian, S. Molana, K. Rahmani, et al., A review on solar chimney systems, Renew. Sustain. Energy Rev. 67 (2017) 954–987.
[10] P.H. Guo, J.Y. Li, B. Xu, et al., Questions and current understanding about solar chimney power plant: a review, Energy Conversion Manag. 182 (2019) 21–33.
[11] N. Pasumarthi, S.A. Sherif, Experimental and theoretical performance of a demonstration solar chimney model—part I: mathematical model development, Int. J. Energy Res. 22 (3) (1998) 277–288.
[12] M.M. Padki, S.A. Sherif, On a simple analytical model for solar chimneys, Int. J. Energy Res. 23 (1999) 345–349.
[13] A.J. Gannon, T.W. von Backström, Solar chimney cycle analysis with system loss and solar collector performance, Sol. Energy Eng. 122 (2000) 133–137.
[14] M.A.D.S. Bernardes, A. Vob, G. Weinrebe, Thermal and technical analyses of solar chimneys, Solar Energy 75 (6) (2003) 511–524.
[15] J.P. Pretorius, D.G. Kröger, Solar chimney power plant performance, J. Solar Energy Eng. 128 (3) (2002) 302.
[16] M.A.dos.S. Bernardes, T.W.von Backström, D.G. Kröger, Critical evaluation of heat transfer coefficients applicable to solar chimney power plant collectors, ISES Sol. World Congr. 3 (2007) 1706–1713.
[17] X. Zhou, J. Yang, B. Xiao, et al., Simulation of a pilot solar chimney thermal power generating equipment, Renew. Energy 32 (10) (2007) 1637–1644.
[18] J.Y. Li, P.H. Guo, Y. Wang, Effects of collector radius and chimney height on power output of a solar chimney power plant with turbines, Renew. Energy 47 (2012) 21–28.
[19] H. Pastohr, O. Kornadt, G. Klaus, Numerical and analytical calculations of the temperature and flow field in the upwind power plant, Int. J. Energy Res. 28 (6) (2004) 495–510.
[20] G. Xu, T. Ming, Y. Pan, F. Meng, C. Zhou, Numerical analysis on the performance of solar chimney power plant system, Energy Convers. Manag. 52 (2011) 876–883.
[21] R. Sangi, M. Amidpour, B. Hosseinizadeh, Modeling and numerical simulation of solar chimney power plants, Sol. Energy 85 (2011) 829–838.
[22] F. Cao, L. Zhao, H. Li, L. Guo, Performance analysis of conventional and sloped solar chimney power plants in China, Appl. Therm. Eng 50 (2013) 582–592.
[23] H.F. Fasel, F. Meng, A.G. Ehsan Shams, CFD analysis for solar chimney power plants, Solar Energy 98 (pt.A) (2013) 12–22.
[24] W. Shen, T. Ming, Y. Ding, Y. Wu, R.K. de-Richter, Numerical analysis on an industrial-scaled solar updraft power plant system with ambient crosswind, Renew. Energy 68 (2014) 662–676.
[25] S.M. Yang, W.Q. Tao, in: Heat Transfer, 4th edition, Higher Education Press, Beijing, 2006, p. 419. page.
[26] M.H. Huang, L. Chen, Y.L. He, W.Q. Tao, A two-dimensional simulation method of the solar chimney power plant with a new radiation model for the collector, Int. Commun Heat Mass Transf. 85 (2017) 100–106.
[27] P.H. Guo, J.Y. Li, Y. Wang, Numerical simulations of solar chimney power plant with radiation model, Renew. Energy 62 (2014) 24–30.
[28] P.H. Guo, J.Y. Li, Y.F. Wang, Y. Wang, Numerical study on the performance of a solar chimney power plant, Energy Convers Manage 105 (2015) 197–205.
[29] E. Gholamalizadeh, M.H. Kim, Three-dimensional CFD analysis for simulating the greenhouse effect in solar chimney power plants using a two-band radiation model, Renew. Energy 63 (2014) 498–506.
[30] Q.H. Wang, J.L. Zhu, X.L. Lu, Numerical simulation of heat transfer process in solar enhanced natural draft dry cooling tower with radiation model, Appl. Therm. Eng. 114 (2017) 977–983.
[31] M.A.H. Abdelmohimen, S.A. Algarni, Numerical investigation of solar chimney power plants performance for Saudi Arabia weather conditions, Sustain. Cities Soc. 38 (2018) 1–8.
[32] L.B. Hooi, S.K. Thangavelu, A parametric simulation of solar chimney power plant, Mater Sci Eng 297 (2018) 012057.
[33] O.A. Najm, S. Shaaban, Numerical investigation and optimization of the solar chimney collector performance and power density, Energy Convers. Manage 168 (2018) 150–161.
[34] A.B. Kasaeian, S. Molana, K. Rahmani, et al., A review on solar chimney systems, Renew Sustain. Energy Rev. 67 (2017) 954–987.
[35] W. Haaf, Solar chimneys part II: preliminary test results from the Manzanares pilot plant [J], Int. J. Sustain. Energy 2 (1984) 141–161.
[36] Q. Cao, T.H. Kuehn, L. Shen, et al., Urban-scale SALSCS, part I: experimental evaluation and numerical modeling of a demonstration unit, Aerosol Air Qual. Res. 18 (11) (2018) 2865–2878.
[37] D.D. Gray, A Giorigin, The validity of the Bussinesq assuption for liquid and gases, Int. J. Heat Mass Transf. 19 (1976) 545–551.
[38] W.Q. Tao, Numerical Heat Transfer, 2nd ed., Xi'an Jiaotong University Press, Xi'an, China, 2001.
[39] ANSYSANSYS FLUENT 14.0 Theory Guide, ANSYS, Inc., 2014.
[40] C.L. Wang, Calculating the parameters that relate to the sun in calculation model of the ionosphere electron concentration, J. China Acad. Electron. Inf. Technol. 8 (1) (2013) 86–90.